

# High Photocurrent and Quantum Efficiency of Graphene Photodetector Using Layer-by-Layer Stack Structure and Trap Assistance

Hua-Min Li, Tian-Zi Shen, Dae-Yeong Lee, and Won Jong Yoo\*

Samsung-SKNU Graphene Center (SSGC), SKNU Advanced Institute of Nano-Technology (SAINT)

Sungkyunkwan University, Suwon 440-746, Korea

\*Phone: 82-31-290-7468, Fax: 82-31-299-4119, Email: [yoowj@skku.edu](mailto:yoowj@skku.edu)

## Abstract

Two approaches, graphene stack (GS) structure assembled by layer-by-layer (LBL) transfer and trap assistant technique for single-layer graphene (SLG), are applied to field-effect transistors (FETs) for photodetection. In LBL-GS-FET, about 3.6 times increased photocurrent (PC) together with increased internal/external quantum efficiency ( $IQE/EQE$ ) is obtained compared to the conventional SLG-FET, owing to an improvement of both electrical transport and optical absorption. In trap-assisted SLG-FET, the PC over 12% compared to the dark current with the superior photoresponsivity ( $S$ ) of 2.8 mA/W and the  $IQE/EQE$  of 23.0%/0.5% is obtained, due to the different response of trapping effect in dark and illumination environments.

## Introduction

Optoelectronics as one of the most promising applications for graphene has attracted strong attention due to the combination of both unique optical and electronic properties (1). However, high efficiency of light-to-current conversion becomes a critical challenge for the rise of graphene optoelectronics currently due to the relatively low PC generation limited by its photon absorbing capacity (2.3%) for a single atomic layer (2), (3). Though various methods have been proposed, e.g., asymmetric metallization (4), surface plasmon resonance (SPR) (2), (3) and hot electron assistance (5), (6) etc, the improvement of photoresponse in graphene optoelectronics is still limited due to the relatively high channel resistance and low optical absorbance. In this work, both the LBL-GS structure and trap assistant technique are proposed as two effective approaches for high efficiency graphene photodetectors. The LBL-GS-FET retains the electron-hole ( $e-h$ ) ambipolar transport characteristics while providing ~3.6 times higher PC,  $IQE$  and  $EQE$  than the conventional SLG-FET, owing to (i) the improved electrical transport, e.g., carrier mobility (4.1 times higher), sheet resistance (61% reduced) and contact resistance (81% reduced) etc, and (ii) the increased optical absorption (over fivefold higher in the visible spectrum). From the trap-assisted SLG-FET, the ultrahigh PC signal was obtained due to the different response of trapping effect under the dark and illumination environments. The PC takes a high proportion over 12% compared to the referential dark current, and its maximum is over 8.5 times higher than the conventional photovoltaic (PV) and photothermoelectronic (PTE) PCs, showing  $S$  of 2.8 mA/W and  $IQE/EQE$  of 23.0%/0.5%. Both of these approaches are demonstrated to effectively improve the optoelectronic performance of graphene photodetectors.

## Device Fabrication and Measurements

The SLG is synthesized on Cu foil via metal catalytic chemical vapor deposition (CVD) (7), and applied to the back-gate FET devices, as described in Fig. 1. In addition to the SLG-FET, 2-layer (2L) and 3-layer (3L) GS structures which are assembled by the LBL transfer of SLG are used in GS-

FETs. The schematic view and microscopic images of a 3L-GS-FET are shown in Fig. 2. The PC signal is defined as the difference of drain current ( $I_D$ ) under the dark and laser (655 nm, 15 mW) illuminating environments at certain drain  $V_D$  and  $V_G$  with various sweep rates (24–360 V/s).

## Layer-by-Layer Graphene Stack Photodetector

As the layer number increases, multi- or few-layer graphene structure exfoliated from highly oriented pyrolytic graphite (HOPG) crystals changes the physical properties, e.g., variation of linear dispersion, opening of bandgap and degradation of carrier mobility etc, due to the  $\pi$  bonds between the  $ABAB$ -ordered layers (8)–(10). As a comparison, the graphene in LBL-GS structure is only vertically stacked via a transfer process, and the absence of  $\pi$  bonds is clearly demonstrated via Raman spectroscopy and X-ray photo-electron spectroscopy (XPS) (9), (10), as shown in Fig. 3(a) and (b). In this case, the Dirac point and ambipolar transport properties are retained in the LBL-GS structure, being similar to those of the SLG, as shown in Fig. 3(c).

The LBL-GS-FET illustrates a significant enhancement of electrical transport, as shown in Fig. 4. The channel resistance ( $R_{ch}$ ) which is maximized at  $V_G$  of the Dirac point ( $V_{Dirac}$ ) due to the minimization of carrier density is drastically reduced from 6.3 k $\Omega$  for SLG to 561  $\Omega$  for 3L-GS, owing to a resistor network (or parallel conducting channel) of GS structure where the absence of  $ABAB$ -order coupling contributes to the reduction of total resistance in LBL-GS structure (9)–(11) (see Fig. 4(a)). The field effect mobility ( $\mu_{eff}$ ) of hole carrier in LBL-GS structure is obtained as a function of carrier density ( $n$ ) (8), which maximum (732 cm $^2$ V $^{-1}$ s $^{-1}$  for 3L-GS) is 4.1 times increased compared to that of the SLG (180 cm $^2$ V $^{-1}$ s $^{-1}$ ) (see Fig. 4(b)). In addition, the sheet and contact resistances of 3L-GS are 617  $\Omega$ /sq and 222  $\Omega$ , which are 61% and 81% suppressed compared to those of the SLG (1.6 k $\Omega$ /sq and 1.2 k $\Omega$ ), respectively, suggesting an improvement of electrical transport induced by the interlayer decoupling effect of misaligned graphene (9), (10) and the shadowing effect of side contact (12) (see Fig. 4(c)).

It is found that  $V_{Dirac}$  shifts to the positive  $V_G$  direction as the number of stacking layer increases (see Fig. 3(c)), showing a *p*-type doping effect in the LBL-GS structure. This is attributed to the accumulation of negative charges and moisture trapped in the graphene during the LBL transfer process (13). Its influence on the optoelectronic performance is interpreted via the shift of the Fermi level ( $E_F$ ) and the built-in potential ( $E_{bi}$ ), as shown in Fig. 5. On one hand, the graphene contact with Al electrode is doped into *n*-type with the shift of  $E_F$  for 0.44 eV ( $\Delta\varphi$ ) relative to the Dirac point energy ( $E_{Dirac}$ ) due to the carrier transfer and chemical interaction (14). On the other hand, the shift of  $E_F$  in the bulk graphene channel ( $\Delta E$ ) relative to  $E_{Dirac}$  is capacitively controlled by  $V_G$ . Therefore, the entire graphene channel is divided into the metal doping region, the bulk channel region and the transition region between the other two (13). As the number of stacking layer increases,  $\Delta E$  is increased from

0.25 eV for SLG to 0.27 eV for 3L-GS (at  $V_D = 0.06$  V and  $V_G = -40$  V), giving rise to a higher  $E_{bi}$  which is defined as  $\Delta E - \Delta\varphi$  and  $\Delta E - \Delta\varphi + qV_D$  at the source and drain transition regions, respectively. The increase of  $E_{bi}$  accelerates the separation of photon-excited  $e-h$  pairs in the transition region and thus enhances the PC generation in graphene.

Optical properties of the LBL-GS structure are investigated with a transparent glass substrate. The average absorbance of 3L-GS in the visible spectrum is 7.0%, being 5.3 times higher than that of the SLG (1.32%), as shown in Fig. 6(a). The laser scanning measurement indicates that the PC is generated only at the graphene near the source and drain contacts (13), as shown in Fig. 6(b). Consequently, owing to the improvement of both electrical transport and optical absorption, the 2L- and 3L-GS-FETs show the outstanding PC,  $S$ ,  $IQE$  and  $EQE$  (2.5  $\mu$ A, 0.17 mA/W, 1.38% and 0.03% for 2L-GS, 3.9  $\mu$ A, 0.26 mA/W, 2.15% and 0.05% for 3L-GS), which are ~2.3 and ~3.6 times increased compared to those of the SLG (1.1  $\mu$ A, 0.07 mA/W, 0.61% and 0.01%), respectively, as shown in Fig. 6(c).

### Trap-Assisted Single-Layer Graphene Photodetector

A distortion of carrier transport which is dependent on the sweep direction, rate and gate voltage is observed clearly in the hole branch of SLG-FET, as shown in Fig. 7(a) and (b). This reduction of channel current has several features. (i) It occurs at the beginning of the forward sweep and in the certain range of the reverse sweep. (ii) It is constant in the forward sweep while enhanced in the reverse sweep as the sweep rate increases. (iii) It is no longer dependent on sweep direction and rate under the illumination environment.

Therefore, a new model on the response of trapping effect for different sweeping environments is proposed as follows. (i) Trap distribution. Based on the  $V_G$ -dependent  $\Delta E$  which is estimated from the  $V_{Dirac}$  (50 V), the range of trapping effect (from -100 to 0 V of  $V_G$ ) in the reverse sweep suggests the corresponding location of hole trap energy levels at 0.18–0.31 eV below  $E_{Dirac}$ . (ii) Complete activation and gradual activation. When the forward sweep starts from  $V_G$  of -100 V, all the hole traps above  $E_F$  are activated completely as  $V_G$  is applied, resulting in a sudden reduction of hole carrier density at the beginning of the forward sweep, as shown in Fig. 7(c). However, when the reverse sweep starts from  $V_G$  of +100 V, the hole traps are activated gradually as  $E_F$  shifts, resulting in a continuous reduction of carrier density in a relatively larger range of  $V_G$ . (iii) Illumination effect. The photons from laser illumination (655 nm) can provide an additional energy (~1.89 eV) to help the holes overcome the capture by the traps, doing away with the trapping effect in neither the forward nor reverse sweeps under the illumination environment. (iv) Trapping and detrapping time ( $\tau_{trap}$ ). A slow transition of  $I_D$  under dark environments ( $I_{D,dark}$ ) is observed during the step pulse measurement, suggesting a long  $\tau_{trap}$  of ~0.18 s. Therefore, the fast sweep cannot allow the charge balance after trapping, and the trapping effect is enhanced as the sweep rate increases (15). (v) Trap density ( $n_{trap}$ ). The  $V_G$ -dependent  $n_{trap}$  can be estimated as the reduction of carrier density ( $\Delta n$ ) (16) by applying different amplitudes of step pulse (-100, -80, -60, -40 and -20 V of  $V_G$ ), as shown in Fig. 7(d) and (e). The maximum  $n_{trap}$  ( $5.8 \times 10^{11} \text{ cm}^{-2}$ ) is obtained at  $V_G$  of -40 V (corresponding to 0.24 eV below  $E_{Dirac}$ ), contributing to the maximum trapping effect. Moreover, the  $n_{trap}$  is also consistent with the effective trap density ( $n_{eff}$  of  $4.3 \times 10^{11} \text{ cm}^{-2}$ ) obtained from the shift of  $V_{Dirac}$  between the forward and reverse sweeps (15).

The PC as a function of  $V_G$  for various sweep rates is obtained, as shown in Fig. 8. In the forward sweep, the PC is generated at the beginning of sweep, and its magnitude is independent of the sweep rates due to the complete activation of traps (see Fig. 8(a)). Whereas, the PC in the reverse sweep follows the trap distribution and shows a peak at  $V_G$  of -40 V (see Fig. 8(b)). The maximum PC in the reverse sweep increases with sweep rate, and eventually saturates as sweep rate exceeds ~200 V/s, in contrast to the constant PC in the forward sweep (see Fig. 8(c)). The trap-assisted maximum PC (41.7 uA) is over 8.5 times higher than the PV and PTE PC (4.9 uA) which location and magnitude are barely affected by the sweep direction and rate. It takes a high proportion of 12.3% compared to the corresponding referential dark current (0.34 mA), showing the superior  $S$  of 2.8 mA/W and  $IQE/EQE$  of 23.0%/0.5%.

In summary, both the LBL-GS structure and trap assistance technique are considered as the new effective approaches to enhance the photoresponse of graphene, compared to the other methods, as listed in Table I.

### Conclusion

In this work, the LBL-GS structure and trap assistance technique have been proposed as the effective approaches for high efficiency graphene optoelectronics, owing to the enhancement of electrical transport and optical absorption as well as the different response of trapping effect under the dark and illumination environments.

### References

- (1) F. Bonaccorso, Z. Sun, T. Hasan, and A. C. Ferrari, "Graphene photonics and optoelectronics," *Nat. Photo.*, vol. 4, pp. 611-622, Aug. 2010.
- (2) T. J. Echtermeyer *et al.*, "Strong plasmonic enhancement of photovoltage in graphene," *Nat. Commu.*, vol. 2, no. 458, Aug. 2011.
- (3) Y. Liu *et al.*, "Plasmon resonance enhanced multicolour photodetection by graphene," *Nat. Commu.*, vol. 2, no. 579, Dec. 2011.
- (4) T. Mueller, F. Xia, and Ph. Avouris, "Graphene photodetectors for high-speed optical communications," *Nat. Photo.*, vol. 4, pp. 297-301, Mar. 2010.
- (5) N. M. Gabor *et al.*, "Hot carrier-assisted intrinsic photoresponse in graphene," *Science*, vol. 334, pp. 648-652, Nov. 2011.
- (6) D. Sun *et al.*, "Ultrafast hot-carrier-dominated photocurrent in graphene," *Nat. Nanotech.*, vol. 7, pp. 114-118, Jan. 2012.
- (7) K. S. Kim *et al.*, "Large-scale pattern growth of graphene films for stretchable transparent electrodes," *Nature*, vol. 457, pp. 706-710, Feb. 2009.
- (8) F. Schwierz, "Graphene transistors," *Nat. Nanotech.*, vol. 5, pp. 487-496, Jul. 2010.
- (9) T. Yu *et al.*, "Carbon-based interconnect: performance, scaling and reliability of 3D stacked multilayer graphene system," in *IEDM Tech. Dig.*, 2011, pp. 159-162.
- (10) T. Yu, C.-W. Liang, C. Kim, E.-S. Song, and B. Yu, "Three-dimensional stacked multilayer graphene interconnects," *IEEE Electron Device Lett.*, vol. 32, pp. 1110-1112, Aug. 2011.
- (11) Y. Sui, and J. Appenzeller, "Screening and interlayer coupling in multilayer graphene field-effect transistors," *Nano Lett.*, vol. 9, pp. 2973-2977, Jul. 2009.
- (12) K. Nagashio, T. Nishimura, K. Kita, and A. Toriumi, "Systematic investigation of the intrinsic channel properties and contact resistance of monolayer and multilayer graphene field-effect transistor," *Jpn. J. Appl. Phys.*, vol. 49, no. 051304, May 2010.
- (13) F. Xia *et al.*, "Photocurrent imaging and efficient photon detection in a graphene transistor," *Nano Lett.*, vol. 9, pp. 1039-1044, Feb. 2009.
- (14) P. A. Khomyakov *et al.*, "First-principles study of the interaction and charge transfer between graphene and metals," *Phys. Rev. B*, vol. 79, no. 195425, May 2009.
- (15) H. Wang, Y. Wu, C. Cong, J. Shang, and T. Yu, "Hysteresis of electronic transport in graphene transistors," *ACS Nano*, vol. 4, pp. 7221-7228, Nov. 2010.
- (16) S. Dimitrijev, *Understanding Semiconductor Devices*, New York: Oxford University Press, 2000, Chap. 5, pp. 249.
- (17) F. Xia, T. Muller, Y.-M Lin, A. Valdes-Garcia, and Ph. Avouris, "Ultrafast graphene photodetector," *Nat. Nanotech.*, vol. 4, pp. 839-843, Dec. 2009.
- (18) B. Chitara, L. S. Panchakarla, S. B. Krupanidhi, and C. N. R. Rao, "Infrared photodetectors based on reduced graphene oxide and graphene nanoribbons," *Adv. Mater.*, vol. 23, pp. 5419-5424, Jul. 2011.
- (19) X. Xu, N. M. Gabor, J. S. Alden, A. M. van der Zande, and P. L. McEuen, "Photo-thermoelectric effect at a graphene interface junction," *Nano Lett.*, vol. 10, pp. 562-566, Nov. 2009.

### Fabrication of SLG- and LBL-GS-FET devices

- CVD growth of SLG on Cu foil
- Spin-coating of polymethyl methacrylate (PMMA)
- Etching of Cu foil in ammonium persulfate
- Washing of PMMA/graphene in DI water
- Transfer to Si substrate with 300-nm-thick  $\text{SiO}_2$
- Drying with flowing  $\text{N}_2$
- Baking on hot plate
- Removal of PMMA in warm acetone
- Patterning of Al electrodes
- Post-annealing in  $\text{N}_2$  atmosphere

LBL transfer  
to assemble  
GS structure

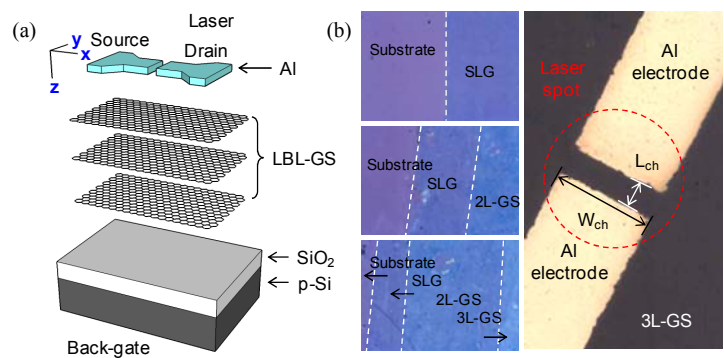


Fig. 1. Fabrication of graphene photodetectors, including the back-gate SLG-FET using CVD synthesized SLG and the back-gate LBL-GS-FET using LBL transfer of CVD synthesized SLG.

Fig. 2. (a) Schematic of LBL-GS-FET under laser illumination. (b) Microscopic images of SLG, 2L-GS, 3L-GS structures, and a 3L-GS-FET device illustrating the length (250  $\mu\text{m}$ ) and width (850 nm) of the channel.

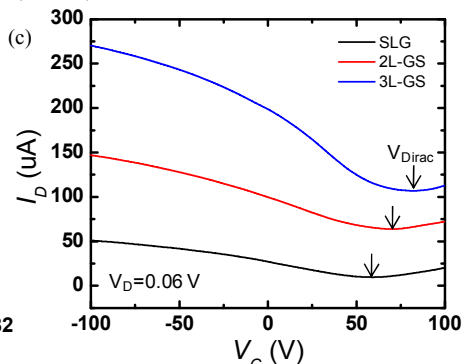
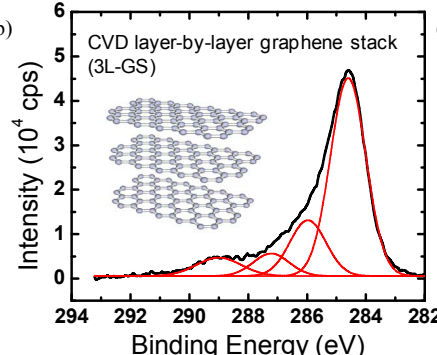
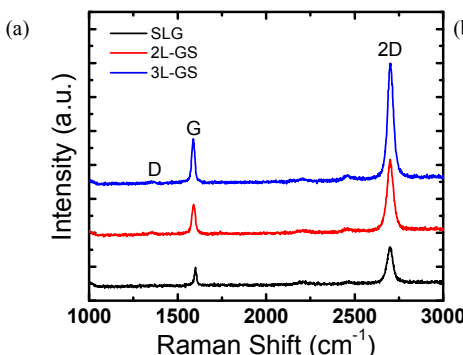


Fig. 3. (a) Raman spectroscopic characterizations (514 nm) of SLG and LBL-GS structure indicate that the intensities of  $G$  and  $2D$  bands increase with a constant ratio as the number of stacking layer increases. (b) XPS characterizations for LBL-GS (3L-GS) indicate an absence of the  $\pi$  bond peak which can be observed at the binding energy of 291.7 eV in the HOPG multi-layer graphene. It only shows a strong  $\sigma$  binding peak at 284.6 eV, being similar to the HOPG multi-layer graphene. (c)  $I_D$ - $V_G$  transfer characteristics of SLG- and LBL-GS-FETs show the Dirac point and ambipolar transport properties.

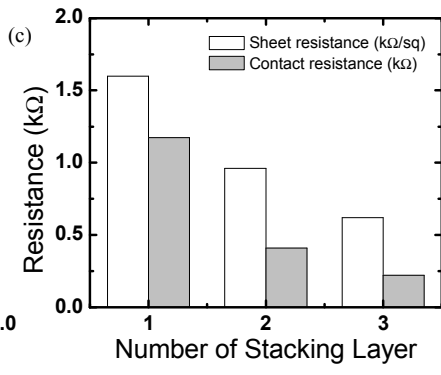
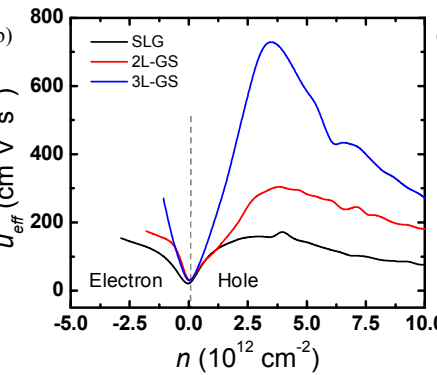
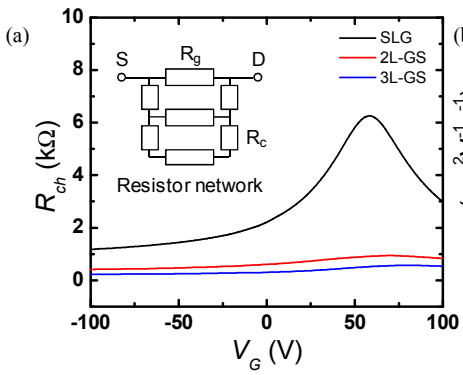


Fig. 4. Electrical transport of SLG- and LBL-GS-FETs, including (a)  $V_G$ -dependent  $R_{ch}$ , (b)  $n$ -dependent  $\mu_{eff}$ , and (c) sheet resistance and contact resistance as functions of the number of stacking layer. Inset of (a): A resistor network (or parallel conducting channel) model of LBL-GS structure interprets the reduction of  $R_{ch}$  as the number of stacking layer increases, where  $S$ ,  $D$ ,  $R_g$  and  $R_c$  denote the source, drain, graphene resistance and contact resistance, respectively.

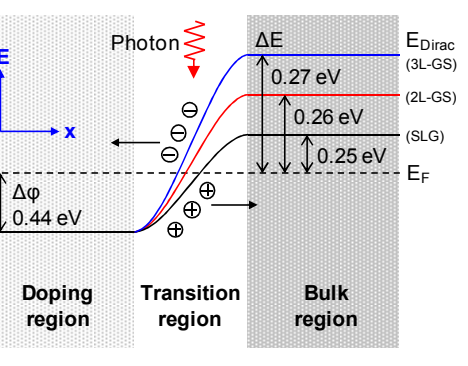
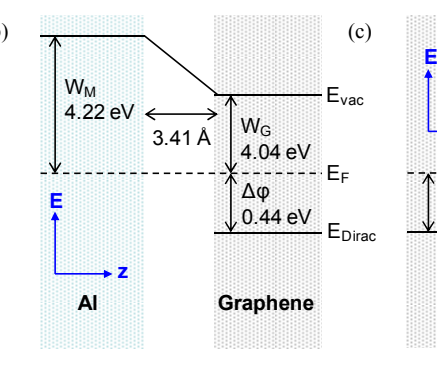
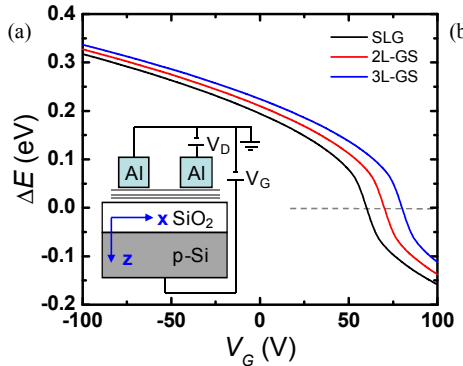


Fig. 5. (a)  $\Delta E$  as a function of  $V_G$  estimated from  $V_{Dirac}$  (see Fig. 3(c)) for SLG- and LBL-GS-FETs. Inset: Cross-sectional view of LBL-GS-FET. (b) Energy band diagram of the graphene-Al interface along the vertical axis ( $z$ ).  $W_M$  and  $W_G$  are the work functions of Al and Al-doped graphene.  $E_{vac}$ ,  $E_F$  and  $E_{Dirac}$  are the vacuum energy, Fermi energy and Dirac point energy, respectively. (c) Energy band diagram of the graphene near the source contact along the horizontal axis ( $x$ ) at  $V_G$  of -40 V.

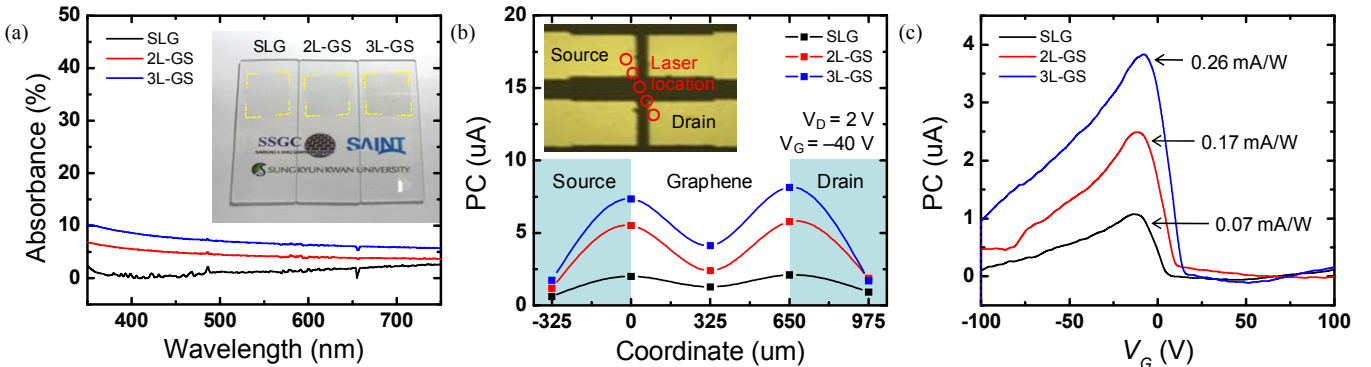


Fig. 6. Optoelectronic performance of SLG- and LBL-GS-FETs, including (a) optical absorbance of the visible spectra, (b) position-dependent PC generation between the source and drain, and (c)  $V_G$ -dependent PC signal and the maximum  $S$ . Inset of (a): Photograph of LBL-GS on glass slide substrates. Inset of (b): Microscopic image illustrates the laser scanning measurement. The red circles denote the laser spot moving from the source to the drain.

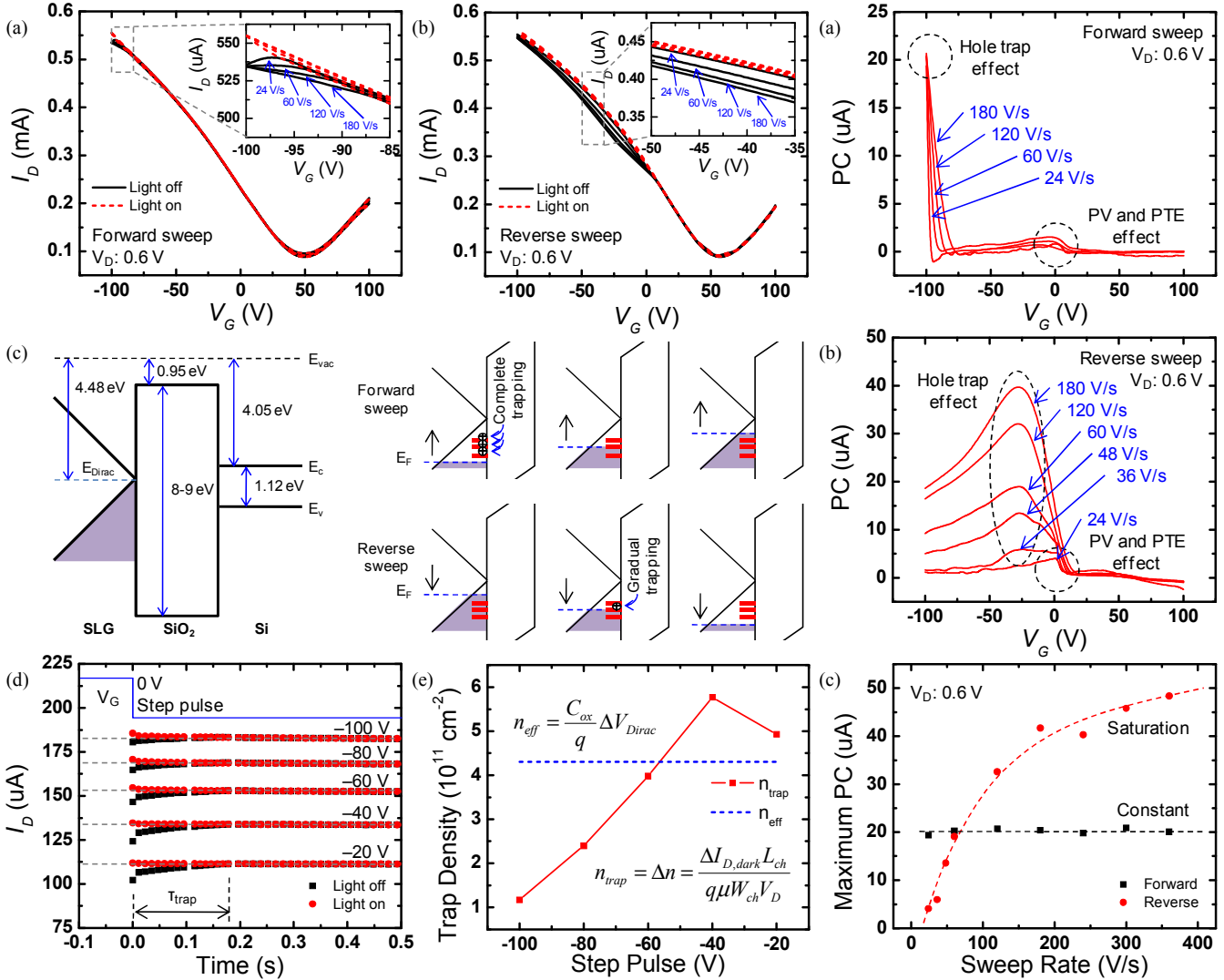


Fig. 7.  $I_D$ - $V_G$  transfer characteristics for (a) forward and (b) reverse sweeps in both dark and illumination environments at various sweep rates. (c) Flat band diagram of graphene-SiO<sub>2</sub>-Si structure and the complete/gradual trapping during forward/reverse sweep, where the red bar denotes hole traps. (d) Step pulse measurement for various amplitudes, indicating a long  $\tau_{trap}$ . (e) Hole trap density and distribution as a function of  $V_G$  estimated from the step pulse measurement (red) and Dirac point shift (blue).

TABLE I. Comparison of the techniques using LBL-GS structure and trap assistance to the other techniques for PC enhancement of graphene

Types	This work: LBL-GS structure (SLG/2L-GS/3L-GS)	This work: Trap assistance	Standard graphene photodetector (17), (18)			Asymmetric metallization (4)		Plasmonic oscillation (2), (3)		Hot carrier- assistance (5)	Single-bilayer junction (19)
Parameter	CVD	CVD	HOPG	RGO	GNR	HOPG		CVD	HOPG		
Graphene <sup>1</sup>	Back-gate	Back-gate	Back-gate	Diode	Diode	Back-gate	Back-gate	Back-gate	Dual-gate	Back-gate	
$S$ (mA/W)	0.07 / 0.17 / 0.26	2.8	0.5	4	1000	6.1	~10	6.1	5	~0.14	
$IQE$ (%)	0.61 / 1.38 / 2.15	23.0	6-16	/	/	~21	/	~65	~32	~1.2	
$EQE$ (%)	0.01 / 0.03 / 0.05	0.5	~0.1-0.4	0.3	80	~0.5	/	1.5	~0.7	~0.03	

<sup>1</sup> CVD: graphene synthesized by CVD; HOPG: graphene exfoliated from HOPG; RGO: reduced graphene oxide; GNR: graphene nanoribbon.

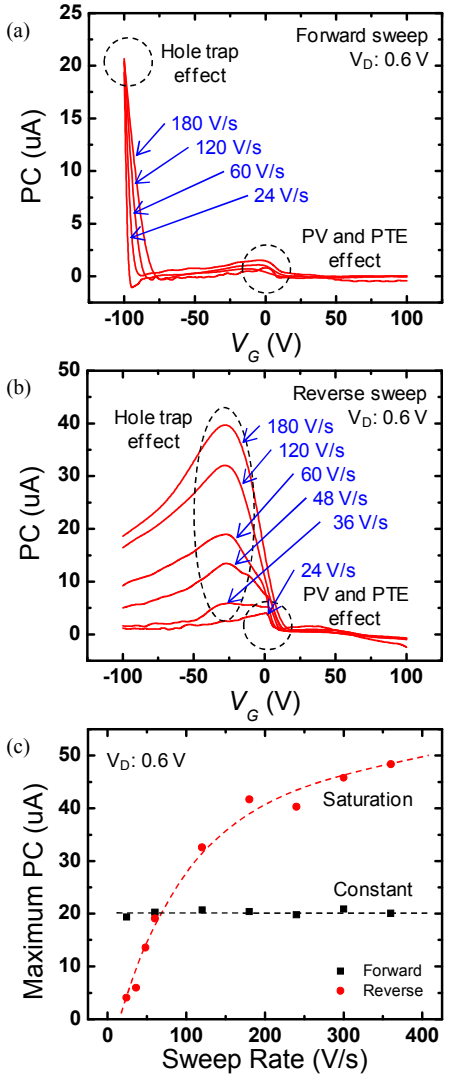


Fig. 8. Trap-assisted PC as a function of  $V_G$  during (a) forward and (b) reverse sweeps at various sweep rates, compared to PV and PTE PC. (c) The maximum PC as a function of sweep rate obtained from forward and reverse sweeps.